

# MeerKAT HI imaging of the jellyfish galaxy ESO 137-001

M. Ramatsoku<sup>1,2,\*</sup>, P. Serra<sup>2</sup>, M. Sun<sup>3</sup>, O.M. Smirnov<sup>1,4,5</sup>, and S. Makhathini<sup>6</sup>

<sup>1</sup> Centre for Radio Astronomy Techniques and Technologies (RATT), Department of Physics and Electronics, Rhodes University, Makhanda, 6140, South Africa.

<sup>2</sup> INAF- Osservatorio Astronomico di Cagliari, Via della Scienza 5, I-09047 Selargius (CA), Italy.

<sup>3</sup> Department of Physics and Astronomy, University of Alabama in Huntsville, 301 Sparkman Drive, Huntsville, AL, 35899, USA.

<sup>4</sup> South African Radio Astronomy Observatory, Black River Park North, 2 Fir St, Cape Town, 7925, South Africa.

<sup>5</sup> Institute for Radioastronomy, National Institute of Astrophysics (INAF IRA), Via Gobetti 101, 40129 Bologna, Italy.

<sup>6</sup> School of Physics, University of the Witwatersrand, Johannesburg, Gauteng, South Africa.

Received 02 October 2024 / Accepted 26 December 2024

## ABSTRACT

We present MeerKAT HI observations of ESO 137-001, a quintessential jellyfish galaxy with long multi-phase tails formed due to the interaction with the intra-cluster medium of its host galaxy cluster, ACO 3627. Our observations reveal the presence of HI in both the disc and outer regions of the galaxy for the first time, with a total HI mass of  $(3.5 \pm 0.4) \times 10^8 M_{\odot}$ . ESO 137-001 is at an advanced stage of gas stripping; it is extremely HI deficient and seems to have lost 90% of its initial HI mass; about 2/3 of the surviving HI is found at larger radius than expected for a normal HI disc and forms  $\sim 40$  kpc tail coincident with the tail detected at other wavelengths. Only  $\sim 10\%$  of the surviving HI is still found within the stellar disc, consistent with the expectation of an outside-in truncation due to ram pressure. Similarly to other jellyfish galaxies, ESO137-001 has a high star formation rate for the low amount of HI detected. We measure an HI depletion time of 0.29 Gyr. However, when taking into account the total gas (HI + H<sub>2</sub>) content, the depletion time is consistent with typical values measured in nearby spiral galaxies. This suggests that ESO 137-001 is at its current stage of ram pressure interaction characterised by an efficient HI stripping, rather than an enhanced conversion of HI to H<sub>2</sub>, which was recently observed in some other jellyfish galaxies.

**Key words.** galaxies: ram pressure stripping, jellyfish galaxy

## 1. Introduction

One of the main objectives of ongoing research into galaxy evolution is to understand the origins and operational mechanisms that lead to the formation of non-star forming early-type galaxies. Higher density galaxy environments such as groups and clusters play a crucial role in this process and are essential to these investigations (Dressler 1980; Postman & Geller 1984; Peng et al. 2010; Whitaker et al. 2012; Foltz et al. 2018). Examples of galaxies transforming due to interactions with their host cluster environment have been reported; these are known as jellyfish galaxies (Yagi et al. 2007; Chung et al. 2009; Smith et al. 2010; Ebeling et al. 2014; Fumagalli et al. 2014; Poggianti et al. 2017a). They form as a result of the hydrodynamical interaction between the intracluster medium (ICM) and the interstellar medium (ISM) as they fall into the cluster centre (e.g. Gunn & Gott 1972). Numerical wind-tunnel simulations have demonstrated that the formation of jellyfish galaxies results from a fast-moving galaxy in a dense ICM. The ram-pressure generated causes the ISM confined by the gravitational potential well of the galaxy to be pushed out of the stellar disc, resulting in highly asymmetric morphologies with extended stripped tails of debris material (Roediger & Brüggén 2008; Kapferer et al. 2009; Ramos-Martínez et al. 2018). The stripped tails have been observed and reported in various wavelengths, including X-ray (Sun & Vikhlinin 2005; Sun et al. 2010; Poggianti et al. 2019), UV and optical wavelengths (Cramer et al. 2019; Yagi et al. 2010; Yoshida et al. 2002), radio continuum (Gavazzi et al.

1995; Crowl et al. 2005; Chen et al. 2020; Roberts et al. 2021), as well as in ionised gas (Yagi et al. 2007; Fossati et al. 2012; Poggianti et al. 2017b; Fossati et al. 2018; Cramer et al. 2019; Fumagalli et al. 2014; Luo et al. 2023), molecular gas (CO; Jachym et al. 2014; Verdugo et al. 2015; Jáchym et al. 2017; Zabel et al. 2019; Moretti et al. 2020, 2023), and neutral atomic gas (HI; Gavazzi 1989; Dickey 1997; Kenney et al. 2004; Chung et al. 2007; Serra et al. 2013; Ramatsoku et al. 2019, 2020; Deb et al. 2020; Loni et al. 2021).

Many jellyfish galaxies have recently been discovered by detecting their ionised gas. This was achieved through extensive surveys, including the Virgo Environmental Survey Tracing Ionised Gas Emission (VESTIGE; Boselli et al. 2018) conducted with the MegaCam instrument on the Canada-France-Hawaii Telescope and the GAs Stripping Phenomena (GASP; Poggianti et al. 2017b) carried out with the Multi Unit Spectroscopic Explorer (MUSE) Integral Field spectrograph on the Very Large Telescope. These galaxies have also been extensively investigated through the LOFAR Two-Meter Sky Survey (LoTSS) in radio continuum (Roberts et al. 2021). Attempts have also been made to understand the properties of jellyfish using the TNG50 gravity+magnetohydrodynamical simulations (Pillepich et al. 2019; Nelson et al. 2019). From these observations and simulations, it has been demonstrated that jellyfish galaxies continue to form stars during the ram-pressure stripping processes, which removes their gas reservoir. Star formation takes place in not only the expected location of galaxy discs but also the stripped tails. Studies have also shown that the ram pressure of most galaxy clusters is generally not strong

\* m.ramatsoku@ru.ac.za

enough to strip the dense star-forming molecular gas, at least not to the extent that would result in the formation of long tails (Lee et al. 2017; Cramer et al. 2020). Instead, the stars in their tails are thought to form in situ from the stripped HI gas that has cooled to a cold and dense phase (Moretti et al. 2020). The question of how star formation can occur given the diffused nature of stripped gas has been explored through studies demonstrating that ordered magnetic fields play a role in facilitating this process (e.g. Etori & Fabian 2000; Asai et al. 2005; Eckert et al. 2017). This was demonstrated for a jellyfish, JO206, in the IIZW108 cluster by Müller et al. (2021) wherein it was reported that magnetic fields prevent momentum exchange and heating, thus shielding the neutral gas and allowing it to cool. The findings of Müller et al. (2021) are partially supported by studies that have reported an efficient conversion of cold and diffuse HI to dense CO gas in jellyfish galaxies (Jachym et al. 2014; Jáchym et al. 2019; Moretti et al. 2020, 2023). However, the complex interplay between gas heating, compression, cooling, and star formation in tails remains poorly understood.

The efficiency of star formation activity in these gas-stripped galaxies remains a topic of ongoing debate. For instance, HI observations conducted on two confirmed jellyfish galaxies detected at optical wavelengths, namely, JO201 and JO206, revealed a coincidence between the spatial distribution and kinematics of H $\alpha$  and HI, as well as enhanced global and resolved star formation activity at kpc-scales in the disc and tail. Simulations which account for galactic winds and cooling found that ram-pressure stripping enhanced the overall SFR in the compressed disc regions and the stripped tail (Kronberger et al. 2008; Kapferer et al. 2009). However, the enhanced SFR is not found in all cases; Deb et al. (2020, 2022) found that in other optically selected jellyfish galaxies, JO204 and JW100, the spatial distribution of HI and H $\alpha$  was distinct, with significant kinematic decoupling observed. Moreover, galaxies undergoing ram-pressure stripping in the Virgo cluster do not have an enhanced star formation rate (Yoon et al. 2017, Brown et al. 2023). In a related study, Mun et al. (2021) used the WISE 22 $\mu$  m flux densities to quantify star formation activity in ram-pressure stripped galaxies, revealing that it is suppressed compared to non-ram-pressure stripped galaxies. Other simulations, including the gravity+magnetohydrodynamical simulations conducted by Göller et al. (2023) on nearly a thousand simulated jellyfish galaxies, have also failed to provide evidence of enhanced SFR for these galaxies.

The differing findings from various studies highlight the lack of a comprehensive understanding of the influence of ram pressure on jellyfish star formation activity. Therefore, reliable measurements of the star formation activity in the bodies and tails remain crucial. Since HI is highly susceptible to ram-pressure stripping and serves as the primary component in the formation of stars, it remains a valuable method for assessing the efficiency of star formation in jellyfish galaxies. However, the limited availability of HI data for these galaxies highlights the need for more in-depth, individual studies to improve our understanding of this process.

ESO 137-001 is one of the most striking jellyfish galaxy undergoing ram-pressure stripping due to its host environment. It is located in the Norma cluster (ACO 3627; Abell et al. 1989) within the Great Attractor region (Dressler et al. 1987). ACO 3627 is a massive structure with a dynamic mass of  $M_{\text{dyn}} \sim 10^{15} M_{\odot}$  at a redshift of  $z = 0.01625$  (Woudt et al. 2008). ESO 137-001 lies near the centre of ACO 3627, at a projected distance of 14.5' ( $\sim 200$  kpc) from the central BCG

galaxy, ESO 137-006 (Sun et al. 2007). Its line-of-sight velocity is  $v = 4647 \text{ km s}^{-1}$  which is a  $200 \text{ km s}^{-1}$  difference from the cluster centre, indicating that it is moving along the plane of the sky (Luo et al. 2023).

This jellyfish galaxy has been extensively observed at various wavelengths. Its initial discovery as a jellyfish was made through X-ray observations conducted with XMM and Chandra (Sun et al. 2006). These observations revealed a long, bifurcated X-ray tail extending from the galaxy disc, with the northern component extending  $\sim 80$  kpc and a shorter southern component. Further observations using the Southern Astrophysical Research (SOAR) telescope revealed an additional 40 kpc H $\alpha$  tail extending from the galaxy disc and pointing away from the cluster centre (Sun et al. 2007). This H $\alpha$  tail was also imaged using the Multi Unit Spectroscopic Explorer (MUSE) on the UT4 Very Large Telescope by Fumagalli et al. (2014) and recently by Luo et al. (2023), who demonstrated that the tail extends much further than previously reported. Its spatial distribution also coincides with the X-ray tail. Within this stripped H $\alpha$  tail, compact, bright knots with the characteristic line ratios, densities, temperatures and metallicity consistent with gas photoionised by young stars were identified (Sun et al. 2010; Fumagalli et al. 2014; Fossati et al. 2016; Luo et al. 2023). The investigation of the star-formation properties of ESO 137-001 using the Infrared Spectrograph (IRS) on the Spitzer Space Telescope revealed a warm H $_2$  20 kpc tail with a mass of  $\sim 10^7 M_{\odot}$  that is aligned with both the X-ray and H $\alpha$  tails (Sivanandam et al. 2010). Follow-up observations with the single dish Atacama Pathfinder Experiment (APEX) revealed CO(2-1) emission in three positions along the 40 kpc H $\alpha$  tail and detected a total H $_2$  mass of  $\sim 10^9 M_{\odot}$  indicating that there is abundant cold, dense gas forming stars in both the disc and tail (Jachym et al. 2014). The Atacama Large Millimeter Array (ALMA) provided high-resolution images of the cold molecular gas traced by CO(2-1) emission in ESO 137-001, revealing a significant amount of this gas phase in both the disc and tail of the galaxy. Its spatial distribution in the tail exhibited clumpy CO overdensities, which likely formed in situ and partly overlapped with HII regions (Jáchym et al. 2019). A detailed study of the star-forming regions was undertaken with Wide Field Camera 3 (WFC3) and the Advanced Camera for Surveys (ACS) on the *Hubble* Space Telescope (HST) in the F275W, F475W, F814W and F160W filters. The data showed a correlation between the HII regions and blue stellar clumps within 0.2 kpc, with the stellar regions measuring a mass of  $\sim 10^4 M_{\odot}$  and ages less than 100 Myr (Waldron et al. 2023).

The amount of CO, ionised gas detected, and young stellar ages in the tail suggest the presence HI. Observations of the HI emission of the host cluster ACO 3627 were conducted with the Australian Telescope Compact Array (ATCA; Frater et al. 1992). Observations were taken with three 30' (FWHM of the ATCA primary beam) pointings within one Abell radius of ACO 3627 ( $1.75^\circ$ ; Woudt et al. 2008) with one of the pointing containing ESO 137-001 centred at the location of the bright central galaxy (BCG) ESO 137-006. They were sensitive to rms noise levels of  $\sim 1 \text{ mJy/beam}$  at a resolution of  $15''$ . However, no HI was detected in ESO 137-001, resulting in an upper limit on the total HI mass of  $\sim 6.0 \times 10^8 M_{\odot}$  at the  $3\sigma$  level for a  $150 \text{ km s}^{-1}$  linewidth (Vollmer et al. 2001).

In this paper, we improve the status of the HI data available for ESO 137-001. The outcomes of our HI observations with MeerKAT (Jonas & MeerKAT Team 2016; Mauch et al.

2020) are presented. We quantify the amount of HI present in ESO 137-001 and examine the spatial distribution of the extraplanar gas in the ram-pressure stripped tail of the galaxy and in the disc. Furthermore, we use the acquired HI data to investigate the correlation between the cold, warm, and hot gas phases and assess the efficiency of star formation under ram-pressure stripping conditions.

The structure of the paper is as follows: In Sect. 2, we present the HI observations and describe the data reduction procedure. The details of the HI source finding procedure and measurements of the total HI content are given in Sect. 3. We compare the HI data to the available multi-wavelength data in Sect. 4. In Sect. 5, we discuss the star formation activity of ESO 137-001 in relation to its gas content and summarise the main results in Sect. 6.

Throughout this paper we adopt a Chabrier (2003) initial mass function (IMF) and assume a  $\Lambda$  cold dark matter cosmology with  $\Omega_M = 0.3$ ,  $\Lambda_\Omega = 0.7$  and a Hubble constant,  $H_0 = 70 \text{ km s}^{-1} \text{ Mpc}^{-1}$ .

## 2. HI observations and data reduction

ACO 3627 was observed with MeerKAT (Jonas & MeerKAT Team 2016; Mauch et al. 2020) in May 2019 (project ID SCI-20190418-SM-01) with 64 antennas using the L-band; 856 – 1712 MHz, for a total of  $2 \times 7$  hours on-source. We used the 4k mode of the SKARAB correlator, which was the only correlator available at the time. It samples the observed band with 4096 channels that are 209-kHz-wide in full polarisation. This resolution was adequate to analyse the spatial distribution of detected HI. Observations were centred on the bright central galaxy (ESO 137-006; Ramatsoku et al. 2020) at  $(\alpha_{J2000}, \delta_{J2000}) = (16\text{h}15\text{m}11\text{s}, -60\text{d}54\text{m}21\text{s})$ , which is about  $14.5'$  from ESO 137-001. This observation scheme was used to mitigate the impact of direction-dependent calibration errors associated with this bright radio source (167 mJy at 1398 MHz; see Ramatsoku et al. 2020). To calibrate the bandpass, complex gains and absolute flux-scale of the instrument, we observed PKS 1934-638 (Jy) for 7 mins after every 60 mins on-source pointings for a total of 1.75 hours.

We processed the data over the frequency range covering the Norma cluster and its background, 1356.620 - 1439.642 MHz, centred at 1398.055 MHz. The  $uv$ -data were reduced using the Containerised Automated Radio Astronomical Calibration (CARACAL; Józsa et al. 2022) pipeline<sup>1</sup>. This data reduction pipeline is built using the radio interferometry framework, STIMELA<sup>2</sup> (Makhathini 2018), which is based on container technologies and Python. The framework supports the combining of various open-source radio interferometry software packages in the same script. The calibrator and target visibilities were flagged with AOFFLAGGER (Offringa et al. 2010) based on the stokes Q visibilities. We used CASA (McMullin et al. 2007) tasks *bandpass* and *gaincal* to determine the antenna-based time-independent complex flux, bandpass and frequency-independent gains, and *fluxscale* was used to bootstrap flux scale and gain amplitudes. The resulting complex gain and bandpass solutions were applied on-the-fly to the target visibilities with the CASA task *applycal* during the splitting of the target visibilities with *mstransform*. ESO 137-001 exhibits a strong, extended continuum emission (see; Koribalski et al. 2024). Furthermore, its

Table 1: Summary of the HI observations.

Property	ESO 137-001
Date	08 and 09 May 2019
Project ID.	SCI-20190418-SM-01
$\alpha$ (J2000)	$16^{\text{h}}15^{\text{m}}03^{\text{s}}.8$
$\Delta$ (J2000)	$-60^{\circ}54'26''.0$
Processed freq. range	(1356 - 1439) MHz
Calibrators:	
Gain, Flux, bandpass	J1939-6342
On-source integration	$2 \times 7$ hrs
HI cube properties	
Channel width	$44.5 \text{ km s}^{-1}$ at $z = 0$
Cube weighting	robust 0.5, taper = $10''$
Sensitivity (r.m.s per channel)	$0.06 \text{ mJy beam}^{-1}$
Restoring Beam (FWHM) (P.A)	$22.3'' \times 16.8''$ ( $150^\circ$ )

proximity to a bright radio galaxy with diffuse, extended lobes necessitated careful continuum subtraction. This step was critical to prevent residual continuum artefacts that could be misinterpreted as faint HI emission within the galaxy (Grobler et al. 2014). To ensure accurate continuum subtraction, we created a model of the continuum sources by imaging and self-calibrating the continuum emission of the target iteratively. The imaging was done with WSCLEAN in Stokes I using multi-scale cleaning (Offringa et al. 2014, Offringa & Smirnov 2017) with the Briggs *robust* weighting parameter set to  $r = 0$  and cleaning down to  $0.5\sigma$  within a clean mask made with sofia (Serra et al. 2015; Westmeier et al. 2021). We self-calibrated the gain phase with CUBICAL (Kenyon et al. 2018) with a solution interval of 128 seconds. The resulting final continuum model was subtracted from the calibrated visibilities with the MSUTILS package. We then subtracted residual continuum emission by fitting a 3rd-order polynomial to the visibilities. This high-order polynomial fit was necessary to sufficiently subtract all the continuum emission. The continuum subtracted  $uv$ -data was then Fourier transformed into a final HI cube with a pixel size of  $2''$  and a field of view of  $1 \text{ deg}^2$ . We used a weighting with Briggs robust parameter,  $r = 0.5$  and  $10''$   $uv$ -tapering to optimise the surface brightness sensitivity. The sidelobes of the synthesised beam were removed by iteratively using SoFia to produce 3D clean masks and imaging with WSCLEAN while cleaning within the masks down to  $0.5\sigma$ . The resulting HI cube has a restoring Gaussian PSF with FWHM of  $22.3'' \times 16.8''$  and a position angle of PA =  $150^\circ$  with an rms of  $\sigma = 0.06 \text{ mJy/beam}$ . With these data, we reach a column density sensitivity of  $N_{\text{HI}} = 2.3 \times 10^{19} \text{ atoms cm}^{-2}$  at  $3\sigma$  at a location of ESO 137-001 in the pointing field assuming a linewidth of  $45 \text{ km s}^{-1}$  (Meyer et al. 2017). A summary of the HI observation and cube properties is listed in Table. 1

## 3. The HI gas emission of ESO 137-001

Our search for the HI emission of ESO 137-001 in the final HI cube was conducted with sofia using the smooth and clip (S+C) method. We employed Gaussian spatial kernels,  $4''$ ,  $12''$ , and  $24''$ , as well as velocity boxcar smoothing kernels of 44 km/s, 132 km/s, and 220 km/s. We set the threshold for accepted HI emission to be brighter than  $3\sigma$  with a reliability of 0.90. The latter is computed by sofia by comparing the distribution of negative and positive sources to distinguish real emission from noise

<sup>1</sup> <https://caracal.readthedocs.io>

<sup>2</sup> <https://github.com/SpheMakh/Stimela>

peaks. The first-ever detection of HI in ESO 137-001 in Fig. 1 shows the extracted HI line emission column density.

We measured a total integrated flux of  $(0.30 \pm 0.03)$  Jy  $\text{km s}^{-1}$  from the HI map shown in Fig. 1. Adopting the luminosity distance reported in Jachym et al. (2014) of  $D = 69.6$  Mpc for ESO 137-001 result in a total HI mass,  $M_{\text{HI}} = (3.5 \pm 0.4) \times 10^8 M_{\odot}$  (Meyer et al. 2017). The uncertainty in the HI mass was calculated through error propagation accounting for the noise of the cube, the number of independent cube voxels included in the HI detection mask, and a 10 per cent flux calibration error (Serra et al. 2023). The measured mass is consistent with the HI mass upper limits from the previous ATCA observations (Vollmer et al. 2001).

### 3.1. HI deficiency

We measured the total amount of HI stripped by ram-pressure by comparing the observed HI mass with the expected, namely, the HI deficiency;  $\text{Def}_{\text{HI}}$  defined by Haynes et al. (1984) as;

$$\text{Def}_{\text{HI}} = \log(M_{\text{HI,exp}}) - \log(M_{\text{HI,obs}}) \quad (1)$$

The expected HI mass was determined using scaling relations based on magnitudes and diameters at optical and near-infrared (NIR) wavelengths, as expressed in equations 5 and 6 of (Dénes et al. 2014). Based on this prescription, galaxies are typically classified as HI-deficient when their  $\text{Def}_{\text{HI}}$  value exceeds 0.6, roughly four times less HI than the average. ESO 137-001 is situated within the Zone of Avoidance at low galactic latitudes, where optical wavelengths suffer dust extinction. To circumvent this issue, we used the galaxy  $K$ -band magnitudes and diameter data obtained from the 2MASS Extended Source Catalog (2MASX; Jarrett et al. 2000). This wavelength is less impacted by dust and has an upper extinction limit of  $A_K = 1.5$  mag at the low galactic latitude of ESO 137-001. The galaxy has an absolute magnitude,  $M_K = -21.97$  mag (Sun et al. 2007) and diameter,  $d_K = 5.5$  arcsec (Skrutskie et al. 2006). Using these and the corresponding fit parameters in Table 2 of Dénes et al. (2014), we measure an expected mass of  $4.6 \times 10^9 M_{\odot}$  and  $5.6 \times 10^9 M_{\odot}$  from the respective magnitudes and diameter based scaling relations. These correspond to  $\text{Def}_{\text{HI}} = 1.12$  and 1.20, respectively. To validate these measurements, we also determined the HI deficiency by comparing the observed HI fraction ( $M_{\text{HI}}/M_*$ ) with the value expected based on the scaling relations derived for field galaxies in the extended GALEX Arecibo SDSS Survey (xGASS; Catinella et al. 2018). In Fig. 2, we compare the observed HI gas fraction with the stacked xGASS scaling relation for galaxies with a stellar surface density comparable to that of ESO 137-001 ( $\log \mu^* = 8.6 M_{\odot}/\text{kpc}^2$ ) (Brown et al. 2015), and with the average HI gas fraction scaling relation (Catinella et al. 2018). ESO 137-001 lies 0.7 - 0.9 dex below the field population. Thus, the expected HI mass of the galaxy is estimated to be up to  $M_{\text{HI}} \approx 2.8 \times 10^9 M_{\odot}$ . These methods indicate a high degree of agreement regarding the fraction of HI gas loss for this galaxy. Using these various techniques, we estimate that the galaxy has generally lost approximately 90% of its initial HI mass.

### 3.2. The HI gas distribution

As shown in Fig. 1, the peak of the HI surface brightness is offset by approximately  $14''$  compared to the centre of the stellar disc. On the east side, the HI distribution is truncated within the stellar disc. The HI truncation is even more pronounced in the south of the stellar disc, potentially due to ram pressure having a

northern component relative to the cluster centre. This is highly likely given the projection of the entire HI distribution. On the west, HI extends significantly beyond the stellar disc, forming a tail that stretches out to about 40 kpc from the galaxy centre. This HI morphology is consistent with the well-established effects of ram-pressure stripping effects on ESO 137-001 by the ICM in the Norma cluster. The entire HI tail is broad, measuring an average of  $\sim 15$  kpc in width in the north-south direction. However, at  $\sim 20$  kpc from the centre of the stellar disc, it becomes more pronounced, widening  $\sim 30$  kpc. Further from the stellar disc, the HI tail narrows to a width of approximately 5 kpc, forming a continuous structure. This may suggest that the galaxy has experienced ram pressure for an extended period, leading to the complete stripping of its outer, low-surface density gas disc. This scenario is plausible, as semi-analytic orbital models indicate the galaxy is roughly 100 Myr before its closest approach, moving at a velocity of  $3000 \text{ km s}^{-1}$  (Jachym et al. 2014).

In Sect. 3.1, we found that ESO 137-001 has lost up to  $\sim 90\%$  of the initial mass. Fig. 1 shows that a significant fraction of its remaining HI is not distributed on a settled disc. To measure how much HI is found at larger distances than expected for a normal HI disc of the same HI mass, we applied the method from Ramatsoku et al. (2019). We built a model assuming that all detected HI is distributed on a settled disc and that ram pressure has not displaced any HI (i.e. no tail has formed). The model exploits the tight correlation between HI mass and galaxy diameter, along with the predictable radial distribution of HI (Wang et al. 2016; Martinsson et al. 2016). Based on the HI size-mass relation parametrised by Wang et al. (2016),  $\log\left(\frac{D_{\text{HI}}}{\text{kpc}}\right) = 0.51 \log\left(\frac{M_{\text{HI}}}{M_{\odot}}\right) - 3.32$ , defined at a surface density of  $1 M_{\odot} \text{pc}^{-2}$ . We used HI surface density radial pro-

file by Martinsson et al. (2016) as:  $\Sigma_{\text{HI}}(R) = \Sigma_{\text{HI}}^{\text{max}} e^{-\frac{(R-R_{\Sigma,\text{max}})^2}{2\sigma_{\Sigma}^2}}$ , where  $R_{\Sigma,\text{max}} = 0.2D_{\text{HI}}$  and  $\sigma_{\Sigma} = 0.18D_{\text{HI}}$  are fixed parameters. The only free parameter is  $\Sigma_{\text{HI}}^{\text{max}}$ , which we set to  $0.4 M_{\odot} \text{pc}^{-2}$  to ensure that  $\Sigma_{\text{HI}}(D_{\text{HI}}/2) = 1 M_{\odot} \text{pc}^{-2}$ . Using these parameters and assuming our observational conditions, we used the 3D-BAROLO package to model the settled HI disc. For the inputs to the model, we assumed a typical HI disc scale height of 0.3 kpc (Randriamampandry et al. 2021), and the position angle and inclination of the stellar disc as listed in Table 1 of Luo et al. (2023). To ensure the model matched our observations, we convolved it with our point spread function (PSF) within 3D-BAROLO. The resulting radius of the model HI disc with  $R_{\text{mod,HI}} = 10$  kpc (semi-major axis) was defined at the HI column density sensitivity of our MeerKAT observations ( $N_{\text{HI}} = 2.3 \times 10^{19}$  atoms  $\text{cm}^{-2}$ ) and is shown in Fig. 1 (grey contour) where it is compared with the observed HI flux density map. Any HI emission in the observed map outside the grey contour is considered part of the HI tail. We measured an HI mass of  $(2.3 \pm 0.2) \times 10^8 M_{\odot}$  within this tail, which accounts for 66% of the total HI mass observed in this galaxy. As shown in Fig. 3, about 50% HI in the tail is concentrated within a projected distance of 20 kpc from the stellar disc, where the tail is broader. In this region, we measure an HI mass of  $M_{\text{HI}} \approx 1.1 \times 10^8 M_{\odot}$ . The rest is spread out beyond this distance, where the tail narrows.

To assess whether the HI morphology is consistent with ram-pressure stripping effects, we identified the approximate radius outside which HI gas has been removed from the stellar disc. This radius, shown by the red ellipse in Fig. 1, is  $\sim 3.6$  kpc (note that this is the observed radius, not deconvolved with the HI resolution; we take care of the effect of resolution as discussed below). Inside this region, we observe an HI mass of

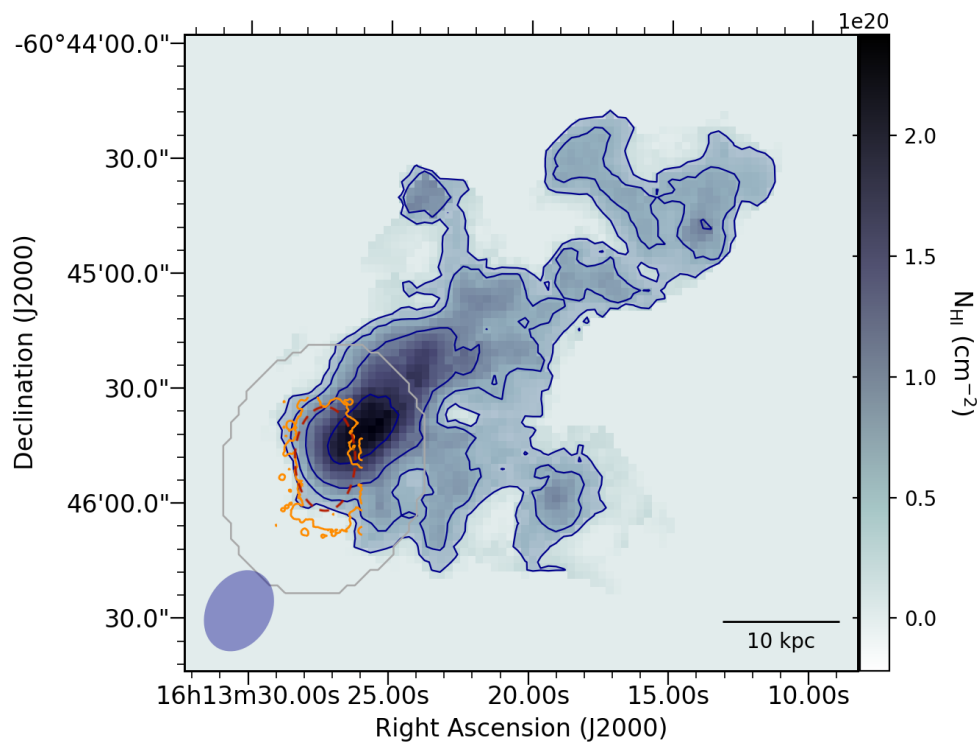


Fig. 1: Integrated HI map of ESO 137-001. The blue contours are at HI column densities of  $2.3, 4.6, 9.2, 18.4 \times 10^{19}$  atoms/cm<sup>2</sup> and the blue ellipse denotes the FWHM beam size of  $22'' \times 16''$  (PA =  $150^\circ$ ). The orange contour represents the galaxy’s optical disc at the 22 mag arcsec<sup>2</sup> isophote in the *r*-band (Fossati et al. 2016). The grey contour outlines a model HI disc defined at the sensitivity limit of our observations,  $N_{\text{HI}} = 2.3 \times 10^{19}$  atoms/cm<sup>2</sup> and the red ellipse delineates the HI stripping radius (see Sect. 3.2).

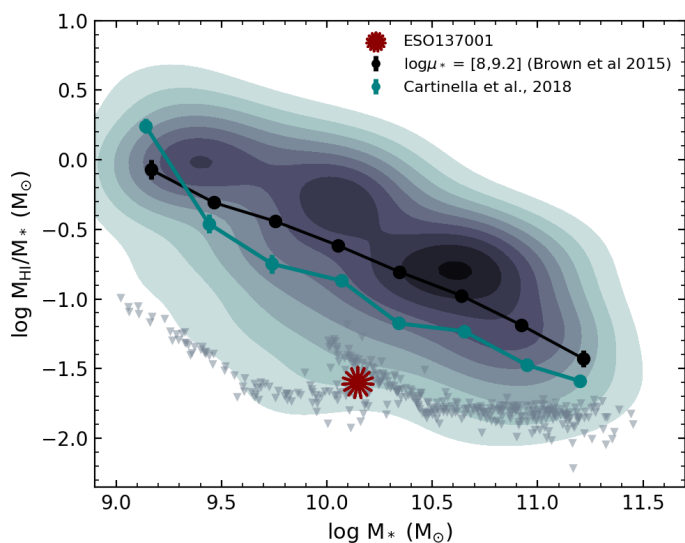


Fig. 2: HI fraction as a function of the stellar mass. Field galaxies from xGASS are shown in grey where the contours are HI detected galaxies, and the triangles represent the non-detections. The xGASS scaling relations based on average gas fraction per stellar mass bin are shown in cyan, while the black points represent galaxies with stellar surface brightness comparable to that of ESO 137-001. The scatter in the mass bins is illustrated by the error bars. ESO 137-001 is represented by the red asterisk.

$(2.7 \pm 0.2) \times 10^7 M_\odot$ , or about 8% of the total observed HI mass in ESO 137-001. Using the modelling approach outlined previously; we assumed an initial (pre-stripping) HI mass of  $2.0 \times 10^9$

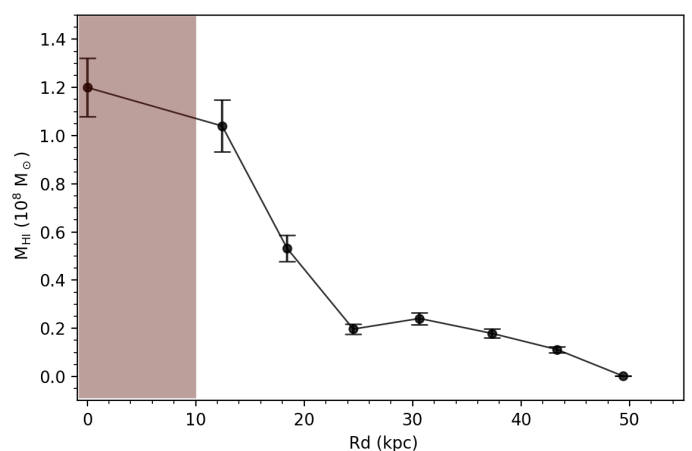


Fig. 3: HI mass measured in 5 kpc bin widths along the HI tail as a function of the projected distance from the centre of the stellar disc of ESO 137-001. The red shaded area indicates the mass within the HI disc.

$M_\odot$  (approximated from scaling relation in Sect.3.1) and measured an extent with a radius of 20.6 kpc for the model disc, defined at our HI column density sensitivity as above. We then truncated this model disc at various radii to simulate gas loss from ram-pressure stripping effects. By convolving each truncated model with the observational PSF, we adjusted the truncation radius until the model matched the red ellipse in Fig. 1. The best match was found with a truncation radius of 1.2 kpc, corresponding to an observed radius of  $\sim 3.9$  kpc after convolution.

Within the truncation radius, the model yielded an HI mass of  $1.1 \times 10^7 M_{\odot}$ ; this matches our observations within a factor of 2. Therefore, the fact that only about 10% of the surviving HI (and about 1% of the initial, expected HI mass) is located within the stellar disc with an observed radius of  $\sim 3.6$  kpc is consistent with the expectation of outside-in truncation due to ram pressure.

#### 4. The HI and the multi-wavelength phases of ESO 137-001

In Fig. 4, we present a comparison of the HI distribution in ESO 137-001 with its X-ray, molecular,  $H\alpha$  emissions, and star-forming regions (Sun et al. 2010; Fumagalli et al. 2014; Jáchym et al. 2019; Waldron et al. 2023). The spatial resolution of HI is generally lower than that of other gas phases, particularly CO and  $H\alpha$ , giving a false impression that the HI distribution is more radially extended. Nonetheless, correlations can still be observed. All gas phases overlap almost entirely within and near the galaxy's stellar disc, where their surface brightness peaks. There is also a strong coincidence between all gas phases throughout the entire 40 kpc long central component of the HI tail. Beyond the HI tail, there is X-ray, CO, and  $H\alpha$  emission. It is possible that the HI in these farthest regions has been transformed into other gas phases or simply lost. This scenario is supported by the presence of a small clump of CO and ionised gas seen extending further than HI. It could also be that the HI is below our detection limit. The clumpy HI protrusions extending perpendicular to the central tail show a local anti-correlation with the perpendicular components of the X-ray and CO emissions. However, X-ray emission is present between these protrusions, possibly tracing trails of stars formed in the galaxy (seen in the HST image), which may have consumed HI in the region. This trend is less pronounced for  $H\alpha$ , where we observe hints of emission that appear to be associated with the HI in these regions. At optical wavelengths, bright young blue star regions with ages less than 10 Myr (see Fig. 5 and Waldron et al. 2023) are found within approximately 10 kpc of the stellar disc and almost overlap with HI emission, particularly in the southern part of the tail. However, in the northern part, there are thin trails of stars that either do not coincide with HI emission or lie just beyond the lowest HI contours. These streams likely originate from molecular gas that formed in situ, as we also observe clumps of CO in those regions that are not linked to any detected HI. No F275W, F475W, and F814W HST band observations are available for comparison beyond 10 kpc from the galaxy centre (Waldron et al. 2023). However, the overlap between HI and  $H\alpha$  suggests star formation activity beyond this distance from the disc.

Figure 6 shows the distribution of the HI emission in velocity channels compared to the CO and  $H\alpha$  emissions. We also show the HI detection mask used to make the intensity map in Fig. 1. Note that since the detection mask was generated from the smoothed cubes (see Sect. 3), some regions may outline emissions below the detection threshold in specific channel maps. To carry out this comparison, the CO cube and  $H\alpha$  data were regridded to have the same velocity resolution as the HI cube. However, due to the relatively low velocity resolution of the HI cube ( $\sim 44$  km s $^{-1}$ ), we can only conduct a qualitative analysis of the general kinematics. Our analysis reveals a significant agreement in velocities between the three gas phases. The HI disc and, more notably, the entire tail emission are seen at a velocity of  $\sim 4655.8$  km s $^{-1}$  with the CO and  $H\alpha$  showing the same velocity distribution. This redshift of all gas phases relative to the stars is consistent with the expected effect of ram pressure given

that the galaxy is blueshifted relative to the ICM (the BCG lies at a velocity of 5444 km s $^{-1}$  (Saraf et al. 2023)).

We also find that within the optical disc, the  $H\alpha$  emission is more extended in velocity by approximately 100 km s $^{-1}$  than HI and CO towards higher and lower velocities. The inner disc emission starts at velocities of  $\sim 4470$  to 4840 km s $^{-1}$ . These regions typically exhibit clumpy HII regions with velocity dispersions of around 30 km s $^{-1}$  (Fossati et al. 2016; Fumagalli et al. 2014; Luo et al. 2023). Outside the optical disc,  $H\alpha$  regions generally show higher velocity dispersions, with diffuse  $H\alpha$  velocities largely consistent with the HI.

#### 5. Gas content and star formation

The star formation rate of ESO 137-001 has been determined from multiple wavelengths. Waldron et al. (2023) derived the total far-infrared luminosity of the galaxy from the *Herschel* data and *Galex* NUV flux density, and estimated a total star formation rate of 0.97  $M_{\odot}$ /yr. Additionally, from the WISE 22  $\mu$  m flux density they estimated a total SFR of 1.39  $M_{\odot}$ /yr. Therefore, the overall average SFR for ESO 137-001 from these estimates is approximately 1.2  $M_{\odot}$ /yr.

We evaluated the star formation rate of ESO 137-001 based on its observed gas content in comparison to similar and previously studied jellyfish galaxies with HI and CO data, namely JO201, JO206, and JW100 (Ramatsoku et al. 2019, 2020; Deb et al. 2022). Our reference field sample is extracted from xGASS for HI and the extended CO Legacy Database for GASS (xCOLDGASS; Saintonge et al. 2017) for molecular gas. To ensure consistency with the jellyfish sample, we recalculated the  $H_2$  mass from xCOLDGASS using a constant CO conversion factor,  $\alpha_{CO, MW} = 4.3$  (K km s $^{-1}$  pc $^2$ ) $^{-1}$ .

In Figure 7, the deviation of the observed star formation rate (SFR) from the main sequence is shown, defined as  $\Delta SFR = \log(SFR/SFR_{ms})$ , and plotted as a function of the deviation of the measured gas fraction ( $f_{gas} = M_{gas}/M_{*}$ ) from the expected,  $\Delta f_{gas} = \log(f_{gas}/f_{gas,exp})$ . We adopt the  $SFR_{ms}$  described by Saintonge et al. (2016);

$$\log SFR = -2.332x + 0.415x^2 - 0.01828x^3 \quad (2)$$

where  $x = \log(M_{*}/M_{\odot})$  and main sequence galaxies are those with  $|\Delta SFR| < 0.4$ . The expected HI and total gas fraction were derived from the xGASS scaling relations (i.e. Figs. 6 & 8 in Catinella et al. 2018). In this  $\Delta SFR$ - $\Delta f_{gas}$  parameter space, the field ('normal') galaxies are on the main sequence, concentrated at  $(\Delta SFR, \Delta f_{gas}) \approx (0,0)$  and are distributed such that the SFR-offset positively correlates with the observed gas fraction offset. The top panel of Fig. 7 shows  $\Delta SFR$  as a function of the HI gas fraction offset  $\Delta f_{HI}$ . In this panel, ESO 137-001 and the comparison jellyfish galaxies lie in the top left quadrant. Although their SFR offset is within the scatter of the main sequence, ESO 137-001 and the other jellyfish galaxies are at the upper edge of the distribution, which indicates a significant excess SFR for their measured HI mass. Indeed, we measure a HI depletion time,  $\tau_{dep} = M_{HI}/SFR$ , of 0.29 Gyr for this galaxy which is much lower than the 2 Gyr value typical for star forming galaxies with a similar stellar mass. In the bottom panel, we show  $\Delta SFR$  as a function of the total (HI +  $H_2$ ) gas fraction deviation,  $\Delta f_{totgas}$ . In this plot ESO 137-001 remains in the top left quadrant with a reduced but still significant offset of  $\log \Delta f_{totgas} = -0.56$ . This is in contrast with the comparison jellyfish galaxies, which have moved to the top right quadrant and are within the scatter of main-sequence galaxies, Moretti et al. (2020, 2023) suggested that this indicates

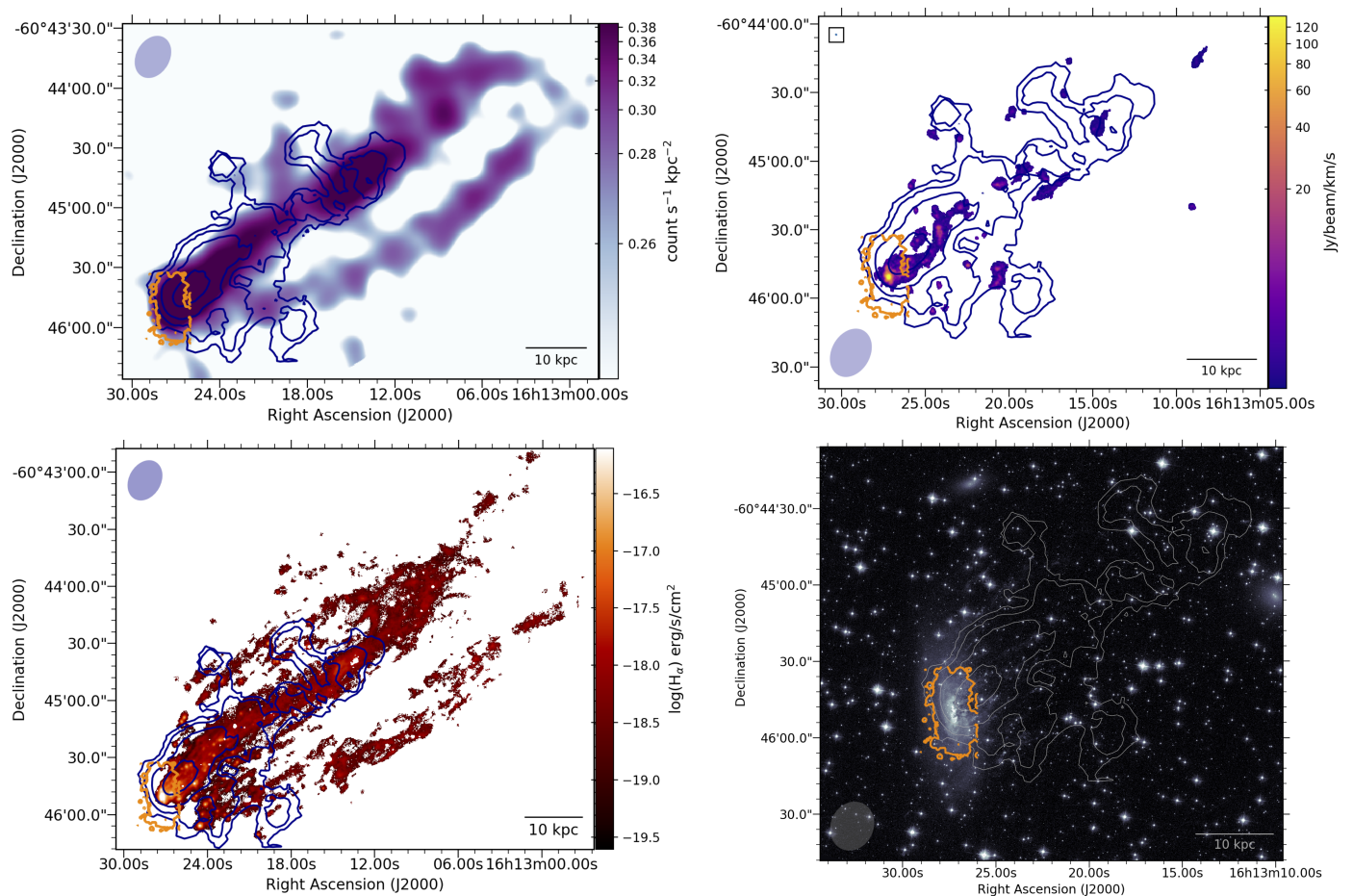


Fig. 4: HI spatial distribution compared to X-ray, CO,  $H\alpha$  and optical maps. The HI contours are drawn at column densities of  $N_{\text{HI}} = 2.3, 4.6, 9.2, 18.4 \times 10^{19}$  atoms/cm<sup>2</sup>. The orange contour is the galaxy disc, as in Fig. 1. *Top left panel:* HI over Chandra 0.6–2.0 keV count X-ray image. *Top right panel:* HI overlaid on the CO (2-1) flux intensity map from ALMA. *Bottom left and right panels:* HI contours over the  $H\alpha$  emission from MUSE and the HST WFC3 image (see also Fig. 1 in Waldron et al. 2023), respectively.

enhanced HI to  $H_2$  conversion during peak stripping. Instead, the position of ESO 137-001 on this plot suggests that this galaxy may be characterised more by efficient HI stripping than by enhanced HI to  $H_2$  conversion. Given its measured star formation rate (SFR) of  $1.2 M_{\odot}/\text{yr}$ , to lie precisely on the main sequence, the galaxy would be expected to have a molecular hydrogen mass  $M_{H_2} = 2.4 \times 10^9 M_{\odot}$  consistent with measurements from ALMA observations (Jáchym et al. 2019).

ESO 137-001 appears to occupy a slightly different region of parameter space in Fig. 7. It has lost much more of its HI compared to its counterparts (see Ramatsoku et al. 2020; Deb et al. 2022). It also has a much lower SFR than its jellyfish counterparts, as shown in Fig. 8. There, we plot the control field sample selected xGASS, consisting of galaxies with stellar masses comparable to ESO 137-001 ( $M_* \sim 1.4 \times 10^{10} M_{\odot}$ ; Sivanandam et al. 2010) spanning one order of magnitude. We also show the jellyfish counterparts. The significant HI deficiency and lower SFR of ESO 137-001 compared to JO201 and JO206, which have a similar stellar mass, indicate that it is at a somewhat more advanced stage in its evolution or that it has experienced increased levels of ram-pressure stripping.

In Fig. 9, we compare the inferred orbital histories or infall times of ESO 137-001 and other jellyfish galaxies within their respective clusters on the phase-space diagram (Jaffé et al. 2015; Rhee et al. 2017). This plot shows the projected distance from

the cluster centre versus the galaxy velocities relative to the cluster. Galaxies fall from large radii at high velocity and eventually settle into the cluster central (i.e. virialised) region delineated by the grey dashed line (Mahajan et al. 2011; Jaffé et al. 2015). The expected ram pressure increases with the ICM density, which increases closer to the cluster centre and with the square of the differential velocity. Jellyfish galaxies are found outside the virialised region at  $r/R_{200} \lesssim 0.6$  travelling at high velocities  $\delta v \geq 1.5\sigma$ . In contrast, ESO 137-001 appears to be located within the virialised region. However, this apparent position largely reflects its motion in the plane of the sky. Like its counterparts, ESO 137-001 is likely falling into the cluster for the first time and is approaching the pericentre.

## 6. Summary

We conducted HI observations of the archetypical jellyfish galaxy, ESO 137-001, located in the nearby massive galaxy cluster, ACO 3627 at  $z = 0.01625$ . It lies near the centre of ACO 3627 at a projected distance of 200 kpc from its centre. ESO 137-001 is undergoing ram-pressure stripping as it falls into the cluster at velocities of  $\sim 3000 \text{ km s}^{-1}$ . Prior ATCA observations did not detect the presence of HI in the galaxy to the upper limit of  $M_{\text{HI}} \sim 6.0 \times 10^8 M_{\odot}$  at the  $3\sigma$  level for a  $150 \text{ km s}^{-1}$  linewidth. The

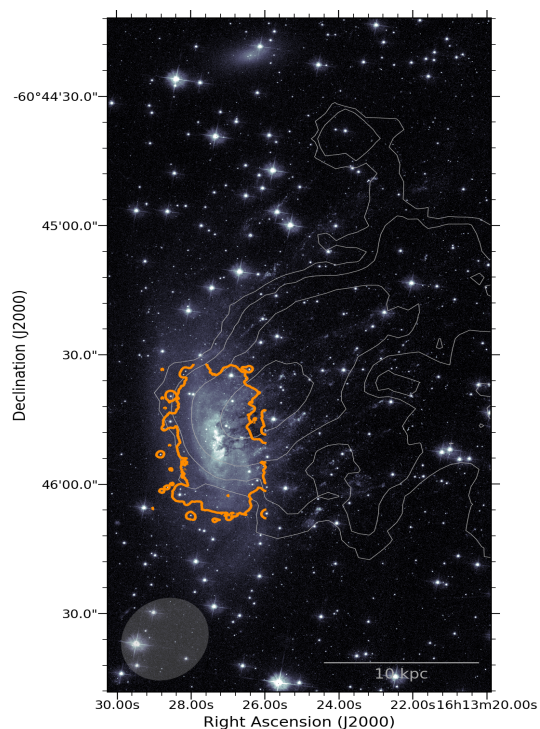


Fig. 5: Zoomed-in image showing trails of young stars close to the galaxy disc with HI contours overlaid on the HST WFC3 image. The orange and grey contour levels are the same as in Fig. 4.

MeerKAT observations enabled the detection of HI in the main body and extended tail of the galaxy for the first time.

We detected HI in the disc and outer regions and measured a total HI mass,  $M_{\text{HI}} = (3.5 \pm 0.4) \times 10^8 M_{\odot}$ . Our analysis revealed that ESO 137-001 is severely HI deficient, having lost  $\sim 90\%$  of its initial HI mass; about  $2/3$  ( $M_{\text{HI}} = 2.3 \times 10^8 M_{\odot}$ ) of the surviving HI is found at a larger radius than expected for a normal gas disc and forms a 40 kpc tail coincident with the tail detected at other wavelengths (e.g. X-ray, CO,  $H\alpha$ ). We also find that  $\sim 10\%$  of the surviving HI is still found within the stellar disc, consistent with the expectation in case of an outside-in truncation due to ram pressure.

ESO 137-001 has a high star formation rate for the amount of HI detected. Our analysis of the SFR in relation to the total gas fraction indicates that ESO 137-001 lies on the upper edge but within the scatter of the SFR main sequence, while the jellyfish galaxies under comparison are situated on the main sequence; the latter typically indicate enhanced HI-to- $H_2$  conversion in jellyfish galaxies during peak ram-pressure stripping reported in recent studies. However, ESO 137-001 appears to be more characterised by efficient HI stripping than enhanced HI-to- $H_2$  conversion, which suggests it might be in an advanced evolutionary stripping phase.

*Acknowledgements.* MR's research is supported by the SARAO HCD programme via the 'New Scientific Frontiers with Precision Radio Interferometry II' research group grant. OMS's research is supported by the South African Research Chairs Initiative of the Department of Science and Technology and the National Research Foundation (grant No. 81737). MS acknowledges the support from the NSF grant 2407821. The authors thank Pavel Jáchym for providing the ALMA CO image. The MeerKAT telescope is operated by the South African Radio Astronomy Observatory, which is a facility of the National Research Foundation, an agency of the Department of Science and Innovation.

Part of the data published here have been reduced using the CARACal pipeline, partially supported by ERC Starting grant number 679629 "FORNAX",

MAECI Grant Number ZA18GR02, DST-NRF Grant Number 113121 as part of the ISARP Joint Research Scheme, and BMBF project 05A17PC2 for D-MeerKAT. Information about CARACal can be obtained online under the URL: <https://caracal.readthedocs.io>.

We acknowledge the use of computing facilities of the Inter-University Institute for Data Intensive Astronomy (IDIA) for part of this work. IDIA is a partnership of the Universities of Cape Town, of the Western Cape and of Pretoria.

## References

- Abell, G. O., Corwin, Jr., H. G., & Olowin, R. P. 1989, *ApJS*, 70, 1
- Asai, N., Fukuda, N., & Matsumoto, R. 2005, *Advances in Space Research*, 36, 636
- Boselli, A., Fossati, M., Ferrarese, L., et al. 2018, *A&A*, 614, A56
- Brown, T., Catinella, B., Cortese, L., et al. 2015, *MNRAS*, 452, 2479
- Brown, T., Roberts, I. D., Thorp, M., et al. 2023, *ApJ*, 956, 37
- Catinella, B., Saintonge, A., Janowiecki, S., et al. 2018, *MNRAS*, 476, 875
- Chabrier, G. 2003, *PASP*, 115, 763
- Chen, H., Sun, M., Yagi, M., et al. 2020, *MNRAS*, 496, 4654
- Chung, A., van Gorkom, J. H., Kenney, J. D. P., Crowl, H., & Vollmer, B. 2009, *AJ*, 138, 1741
- Chung, A., van Gorkom, J. H., Kenney, J. D. P., & Vollmer, B. 2007, *ApJL*, 659, L115
- Cramer, W. J., Kenney, J. D. P., Cortes, J. R., et al. 2020, *ApJ*, 901, 95
- Cramer, W. J., Kenney, J. D. P., Sun, M., et al. 2019, *ApJ*, 870, 63
- Crowl, H. H., Kenney, J. D. P., van Gorkom, J. H., & Vollmer, B. 2005, *AJ*, 130, 65
- Deb, T., Verheijen, M. A. W., Gullieuszik, M., et al. 2020, *MNRAS*, 494, 5029
- Deb, T., Verheijen, M. A. W., Poggianti, B. M., et al. 2022, *MNRAS*, 516, 2683
- Dénes, H., Kilborn, V. A., & Koribalski, B. S. 2014, *MNRAS*, 444, 667
- Dickey, J. M. 1997, *AJ*, 113, 1939
- Dressler, A. 1980, *ApJ*, 236, 351
- Dressler, A., Faber, S. M., Burstein, D., et al. 1987, *ApJL*, 313, L37
- Ebeling, H., Stephenson, L. N., & Edge, A. C. 2014, *ApJL*, 781, L40
- Eckert, D., Gaspari, M., Owers, M. S., et al. 2017, *A&A*, 605, A25
- Ettori, S. & Fabian, A. C. 2000, *MNRAS*, 317, L57
- Foltz, R., Wilson, G., Muzzin, A., et al. 2018, *ApJ*, 866, 136
- Fossati, M., Fumagalli, M., Boselli, A., et al. 2016, *MNRAS*, 455, 2028
- Fossati, M., Gavazzi, G., Boselli, A., & Fumagalli, M. 2012, *A&A*, 544, A128
- Fossati, M., Mendel, J. T., Boselli, A., et al. 2018, *A&A*, 614, A57
- Frater, R. H., Brooks, J. W., & Whiteoak, J. B. 1992, *Journal of Electrical and Electronics Engineering Australia*, 12, 103
- Fumagalli, M., Fossati, M., Hau, G. K. T., et al. 2014, *MNRAS*, 445, 4335
- Gavazzi, G. 1989, *ApJ*, 346, 59
- Gavazzi, G., Contursi, A., Carrasco, L., et al. 1995, *A&A*, 304, 325
- Göller, J., Joshi, G. D., Rohr, E., Zinger, E., & Pillepich, A. 2023, *MNRAS*, 525, 3551
- Grobler, T. L., Nunhokee, C. D., Smirnov, O. M., van Zyl, A. J., & de Bruyn, A. G. 2014, *MNRAS*, 439, 4030
- Gunn, J. E. & Gott, III, J. R. 1972, *ApJ*, 176, 1
- Haynes, M. P., Giovanelli, R., & Chincarini, G. L. 1984, *ARA&A*, 22, 445
- Jáchym, P., Combes, F., Cortese, L., Sun, M., & Kenney, J. D. P. 2014, *ApJ*, 792, 11
- Jáchym, P., Kenney, J. D. P., Sun, M., et al. 2019, *ApJ*, 883, 145
- Jáchym, P., Sun, M., Kenney, J. D. P., et al. 2017, *ApJ*, 839, 114
- Jaffé, Y. L., Smith, R., Candlish, G. N., et al. 2015, *MNRAS*, 448, 1715
- Jarrett, T. H., Chester, T., Cutri, R., et al. 2000, *AJ*, 119, 2498
- Jonas, J. & MeerKAT Team. 2016, in *MeerKAT Science: On the Pathway to the SKA*, 1
- Józsa, G. I. G., Andati, L. A. L., de Blok, W. J. G., et al. 2022, in *Astronomical Society of the Pacific Conference Series*, Vol. 532, *Astronomical Society of the Pacific Conference Series*, ed. J. E. Ruiz, F. Pierfederci, & P. Teuben, 447
- Kapferer, W., Sluka, C., Schindler, S., Ferrari, C., & Ziegler, B. 2009, *A&A*, 499, 87
- Kenney, J. D. P., van Gorkom, J. H., & Vollmer, B. 2004, *AJ*, 127, 3361
- Kenyon, J. S., Smirnov, O. M., Grobler, T. L., & Perkins, S. J. 2018, *MNRAS*, 478, 2399
- Koribalski, B. S., Duchesne, S. W., Lenc, E., et al. 2024, *MNRAS*, 533, 608
- Kronberger, T., Kapferer, W., Ferrari, C., Unterguggenberger, S., & Schindler, S. 2008, *A&A*, 481, 337
- Lee, B., Chung, A., Tonnesen, S., et al. 2017, *MNRAS*, 466, 1382
- Loni, A., Serra, P., Kleiner, D., et al. 2021, *A&A*, 648, A31
- Luo, R., Sun, M., Jáchym, P., et al. 2023, *MNRAS*, 521, 6266
- Mahajan, S., Mamon, G. A., & Raychaudhury, S. 2011, *MNRAS*, 416, 2882
- Makhathini, S. 2018, PhD thesis, Rhodes University, Drosty Rd, Grahamstown, 6139, Eastern Cape, South Africa, available via <http://hdl.handle.net/10962/57348>



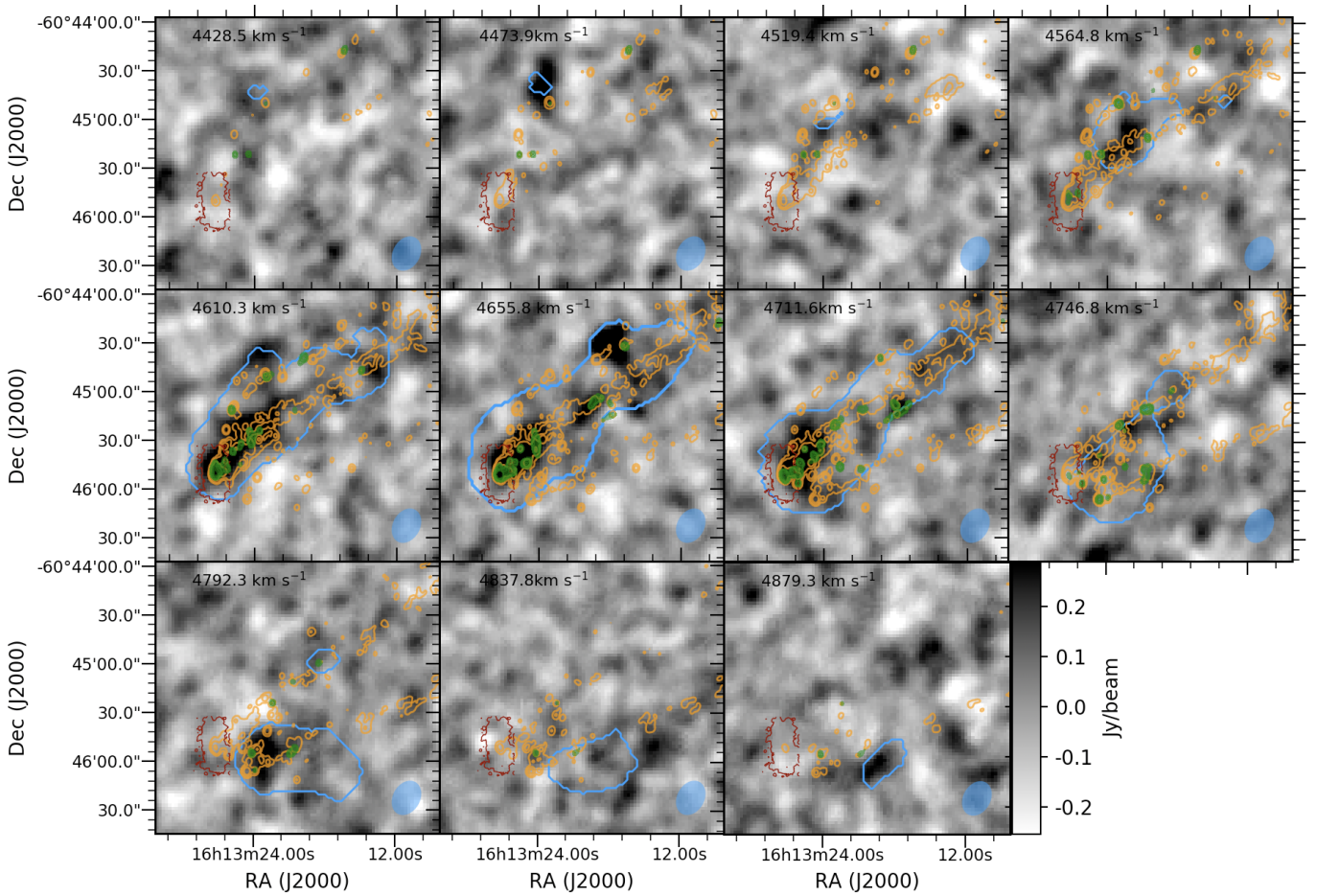


Fig. 6: Channel maps of the HI cube of ESO 137-001 compared with CO and H $\alpha$ . The greyscale is linear and ranges from  $-5\sigma$  to  $5\sigma$  where  $\sigma$  is the rms of the HI cube. Each channel is labelled with the channel velocity. The light blue contours represent the detection mask used to make the HI intensity (zeroth moment) maps. Green and orange contours are CO and H $\alpha$  emission at levels of 0.1, 0.3, 0.6 ... Jy beam $^{-1}$  and 1, 10, 100, ...  $\times 10^{-18}$  erg s $^{-1}$  cm $^{-2}$ , respectively. The red contour is the stellar disc, as shown in Fig 1.

Martinsson, T. P. K., Verheijen, M. A. W., Bershadsky, M. A., et al. 2016, *A&A*, 585, A99  
Mauch, T., Cotton, W. D., Condon, J. J., et al. 2020, *ApJ*, 888, 61  
McMullin, J. P., Waters, B., Schiebel, D., Young, W., & Golap, K. 2007, in *Astronomical Society of the Pacific Conference Series*, Vol. 376, *Astronomical Data Analysis Software and Systems XVI*, ed. R. A. Shaw, F. Hill, & D. J. Bell, 127  
Meyer, M., Robotham, A., Obreschkow, D., et al. 2017, *PASA*, 34, 52  
Moretti, A., Paladino, R., Poggianti, B. M., et al. 2020, *ApJL*, 897, L30  
Moretti, A., Serra, P., Bacchini, C., et al. 2023, *ApJ*, 955, 153  
Müller, A., Poggianti, B. M., Pfrommer, C., et al. 2021, *Nature Astronomy*, 5, 159  
Mun, J. Y., Hwang, H. S., Lee, M. G., et al. 2021, *Journal of Korean Astronomical Society*, 54, 17  
Navarro, J. F., Frenk, C. S., & White, S. D. M. 1996, *ApJ*, 462, 563  
Nelson, D., Pillepich, A., Springel, V., et al. 2019, *MNRAS*, 490, 3234  
Offringa, A. R., de Bruyn, A. G., Biehl, M., et al. 2010, *MNRAS*, 405, 155  
Offringa, A. R., McKinley, B., Hurley-Walker, N., et al. 2014, *MNRAS*, 444, 606  
Offringa, A. R. & Smirnov, O. 2017, *MNRAS*, 471, 301  
Peng, Y.-j., Lilly, S. J., Kovač, K., et al. 2010, *ApJ*, 721, 193  
Pillepich, A., Nelson, D., Springel, V., et al. 2019, *MNRAS*, 490, 3196  
Poggianti, B. M., Ignesti, A., Gitti, M., et al. 2019, *ApJ*, 887, 155  
Poggianti, B. M., Jaffé, Y. L., Moretti, A., et al. 2017a, *Nature*, 548, 304  
Poggianti, B. M., Moretti, A., Gullieuszik, M., et al. 2017b, *ApJ*, 844, 48  
Postman, M. & Geller, M. J. 1984, *ApJ*, 281, 95  
Ramatsoku, M., Serra, P., Poggianti, B. M., et al. 2020, *A&A*, 640, A22  
Ramatsoku, M., Serra, P., Poggianti, B. M., et al. 2019, *MNRAS*, 487, 4580  
Ramos-Martínez, M., Gómez, G. C., & Pérez-Villegas, Á. 2018, *MNRAS*, 476, 3781

Randriamampandry, T. H., Wang, J., & Mogotsi, K. M. 2021, *ApJ*, 916, 26  
Rhee, J., Smith, R., Choi, H., et al. 2017, *ApJ*, 843, 128  
Roberts, I. D., van Weeren, R. J., McGee, S. L., et al. 2021, *A&A*, 652, A153  
Roediger, E. & Brüggem, M. 2008, *MNRAS*, 388, L89  
Saintonge, A., Catinella, B., Cortese, L., et al. 2016, *MNRAS*, 462, 1749  
Saintonge, A., Catinella, B., Tacconi, L. J., et al. 2017, *ApJS*, 233, 22  
Saraf, M., Wong, O. I., Cortese, L., & Koribalski, B. S. 2023, *MNRAS*, 519, 4128  
Serra, P., Koribalski, B., Duc, P.-A., et al. 2013, *MNRAS*, 428, 370  
Serra, P., Maccagni, F. M., Kleiner, D., et al. 2023, *A&A*, 673, A146  
Serra, P., Westmeier, T., Giese, N., et al. 2015, *MNRAS*, 448, 1922  
Sivanandam, S., Rieke, M. J., & Rieke, G. H. 2010, *ApJ*, 717, 147  
Skrutskie, M. F., Cutri, R. M., Stiening, R., et al. 2006, *AJ*, 131, 1163  
Smith, R. J., Lucey, J. R., Hammer, D., et al. 2010, *MNRAS*, 408, 1417  
Sun, M., Donahue, M., Roediger, E., et al. 2010, *ApJ*, 708, 946  
Sun, M., Donahue, M., & Voit, G. M. 2007, *ApJ*, 671, 190  
Sun, M., Jones, C., Forman, W., et al. 2006, *ApJL*, 637, L81  
Sun, M. & Vikhlinin, A. 2005, *The Astrophysical Journal*, 621, 718  
Verdugo, C., Combes, F., Dasyra, K., Salomé, P., & Braine, J. 2015, *A&A*, 582, A6  
Vollmer, B., Cayatte, V., van Driel, W., et al. 2001, *A&A*, 369, 432  
Waldron, W., Sun, M., Luo, R., et al. 2023, *MNRAS*, 522, 173  
Wang, J., Koribalski, B. S., Serra, P., et al. 2016, *MNRAS*, 460, 2143  
Westmeier, T., Kitaëff, S., Pallot, D., et al. 2021, *MNRAS*, 506, 3962  
Whitaker, K. E., van Dokkum, P. G., Brammer, G., & Franx, M. 2012, *ApJL*, 754, L29  
Woudt, P. A., Kraan-Korteweg, R. C., Lucey, J., Fairall, A. P., & Moore, S. A. W. 2008, *MNRAS*, 383, 445  
Yagi, M., Komiyama, Y., Yoshida, M., et al. 2007, *ApJ*, 660, 1209  
Yagi, M., Yoshida, M., Komiyama, Y., et al. 2010, *AJ*, 140, 1814  
Yoon, H., Chung, A., Smith, R., & Jaffé, Y. L. 2017, *ApJ*, 838, 81  
Yoshida, M., Yagi, M., Okamura, S., et al. 2002, *ApJ*, 567, 118  
Zabel, N., Davis, T. A., Smith, M. W. L., et al. 2019, *MNRAS*, 483, 2251

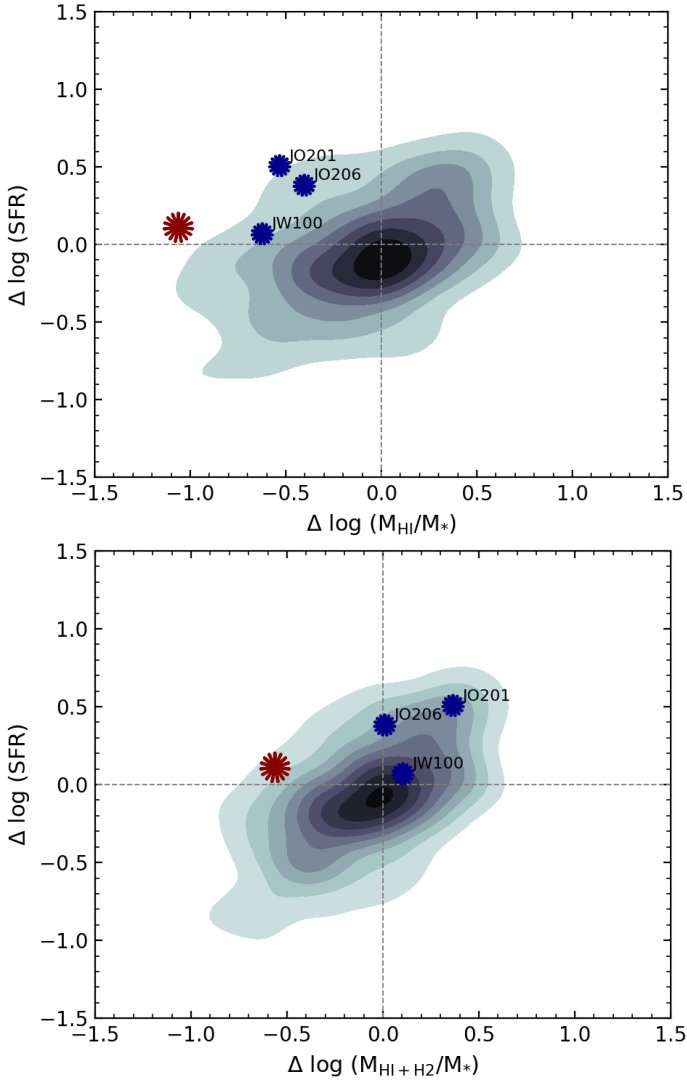


Fig. 7: Star formation rate offset from the main sequence as a function of the H I gas (top) and total gas (bottom) fraction offset from the xGASS gas scaling relations. Grey contours are ‘normal’ field galaxies. The red asterisk represents ESO 137-001, and the blue asterisks show the comparison sample of jellyfish galaxies.

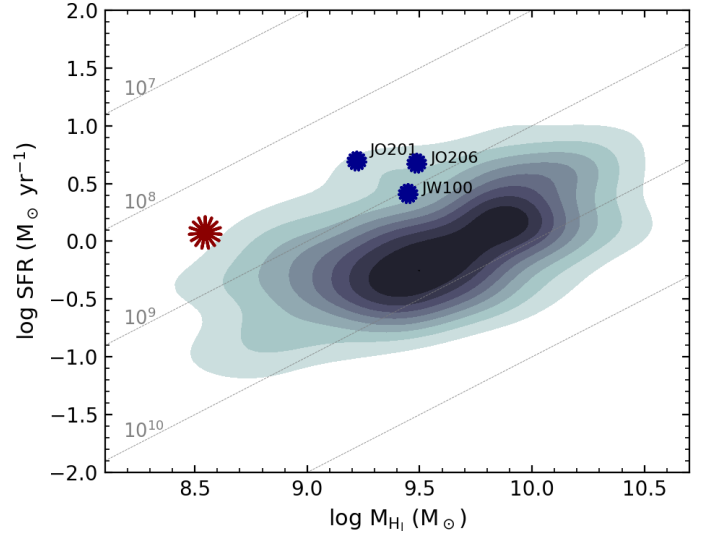


Fig. 8: Star formation rate as function of H I mass for galaxies with similar stellar masses as ESO 137-001 and jellyfish counterparts. Grey contours are galaxies from xGASS. The red asterisk represents ESO 137-001 while the blue points are jellyfish galaxies, JO206, JO201 and JW100.

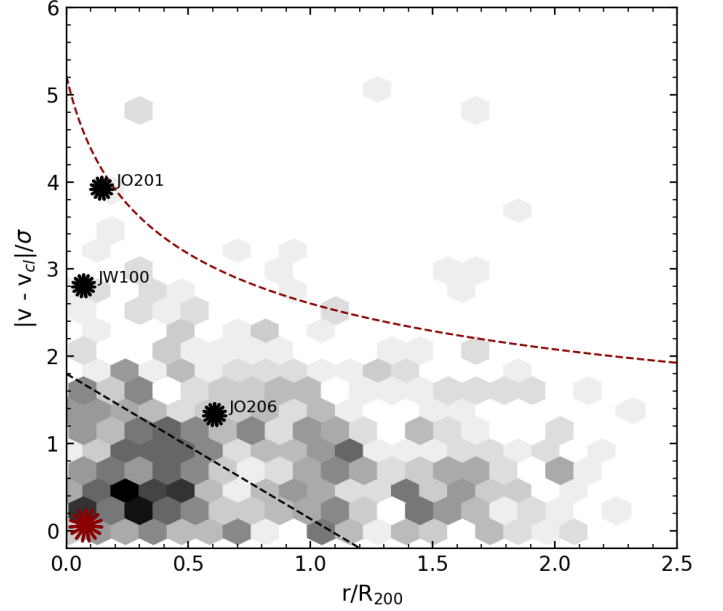


Fig. 9: Composite projected phase-space diagram of spectroscopically confirmed galaxy members of clusters Abell 85, IIZW108, Abell 2626 and ACO 3627 within which the comparison jellyfish galaxies (JO201, JO206, JW100) and ESO 137-001 are located, respectively. The red curve is the escape velocity in an NFW halo (Navarro et al. 1996). The dashed black line indicates the region where galaxies are most likely virialised. Black asterisks are the comparison sample of jellyfish galaxies within their respective galaxy clusters, and the red asterisk represents ESO 137-001.